*photonics*

MDPI

*Article*

# Novel THz Metasurface Biosensor for High-Sensitivity Detection of Vitamin C and Vitamin B9

**Ningyi Wang †, Bingwei Liu †, Xu Wu * and Yan Peng**

Shanghai Key Lab of Modern Optical System, Terahertz Technology Innovation Research Institute, Terahertz Spectral and Imaging Technology National Cooperative Innovation Center, University of Shanghai for Science and Technology, Shanghai 200093, China; 2135062007@st.usst.edu.cn (N.W.); 211180045@st.usst.edu.cn (B.L.); py@usst.edu.cn (Y.P.)

* Correspondence: wuxu@usst.edu.cn

† These authors contributed equally to this work.

**Abstract:** Vitamin C (VC) and Vitamin B9 (VB9) are essential micronutrients integral to numerous biological functions and critical for maintaining human health. The rapid detection of these vitamins is important for verifying nutritional supplements and aiding in clinical diagnoses. This study combined terahertz time-domain spectroscopy (THz-TDS) with metasurface technology to develop a fast, sensitive, and non-destructive detection method for VC and VB9. Firstly, we determined the characteristic absorption peaks and molecular vibration modes of VC and VB9 within the 0.5–4.0 THz range through quantum chemical calculation and THz-TDS measurement. Then, we designed and fabricated a metasurface biosensor to match its resonance peak with the communal peak of VC and VB9, enhancing the interaction between THz waves and these vitamins. Using this biosensor, we analyzed solutions with different concentrations of VC and VB9. An increase in vitamin concentrations resulted in frequency shifts in the THz resonance peak. Quantifiable relationships between frequency shifts and the vitamin concentrations were established. The detection limits achieved were 158.82 ng/μL for VC and 353.57 ng/μL for VB9, respectively. This method not only demonstrates high sensitivity but also simplifies the operational process, offering an innovative tool for applications in food safety monitoring and clinical diagnostics.

**Keywords:** vitamin C; vitamin B9; folic acid; metasurface; terahertz spectroscopy; rapid detection; trace analysis



**Citation:** Wang, N.; Liu, B.; Wu, X.; Peng, Y. Novel THz Metasurface Biosensor for High-Sensitivity Detection of Vitamin C and Vitamin B9. *Photonics* **2024**, *11*, 820. https://doi.org/10.3390/photonics11090820

Received: 10 August 2024
Revised: 28 August 2024
Accepted: 28 August 2024
Published: 30 August 2024



## 1. Introduction

Vitamins are organic compounds essential for sustaining human life processes. They play a key role in regulating metabolism and are found in various foods and nutritional supplements [1,2]. Vitamin C (L-ascorbic acid, VC) and vitamin B9 (folic acid, VB9) are indispensable for the human body. VC is renowned for its diverse biological functions, including anti-inflammatory, antioxidant, and immunomodulatory activities. It is applied in the treatment of inflammatory diseases such as scurvy, sepsis, systemic lupus erythematosus, and rheumatoid arthritis. However, VC cannot be synthesized internally and therefore requires external intake [2]. Excessive VC intake can result in adverse effects such as kidney stones, gastrointestinal discomfort, and iron overload [3–5]. Similarly, VB9 is crucial for metabolism, DNA/RNA synthesis, and cell growth. It plays a critical role in preventing fetal neural tube defects and megaloblastic anemia. Nonetheless, VB9 also cannot be synthesized internally. Excessive VB9 intake may obscure the symptoms of Vitamin B12 deficiency and potentially increase the risk of fetal developmental abnormalities [6–9]. Considering the key role of VC and VB9 in maintaining health, coupled with the health risks associated with their deficiency or excess, the necessity for a rapid and accurate detection method is imperative.

Traditional methods for detecting VC and VB9 include high-performance liquid chromatography (HPLC), electrochemical techniques, and fluorescence analysis. The HPLC method separates and detects components by the distribution equilibrium between stationary and mobile phases, with the advantages of high sensitivity and accuracy. In 2024, Li, H. et al. [10] used HPLC to detect the VC concentration in fruits and vegetables with a limit of detection (LOD) of 0.05 μg/mL.In the same year, Yang, Y. et al. [11] employed HPLC to detect VB9 concentration in multivitamin tablets with a LOD of 0.033 mg/L. Electrochemical methods detect substances by analyzing the changes in potential and current in an electrolytic cell, which is highly sensitive and easy to operate. In 2020, Brainina, K.Z. et al. [12] developed an electrochemical sensor using phytosynthesized gold nanoparticles and carbon veil for VC detection, achieving a LOD of 0.05 μM and a linear range of 1 μM–5.75 mM. In 2018, Kuceki, M. et al. [13] developed an electrochemical sensor using a hybrid molecularly imprinted polymer with a restricted access modified electrode for VB9 detection, achieving a LOD of 0.72 μg/L and a linear range of 5.0–100.0 μg/L. Fluorescence analysis is based on the inherent fluorescence properties of molecules for selective measurement, with the advantages of high sensitivity and a wide linear range. In 2019, Wang, Y. et al. [14] used ratiometric fluorescence methods to detect VC, achieving a LOD of 0.009 μM and a linear range of 0.6–40 μM. In 2020, May, B.M.M. et al. [15] used water-soluble $AgInS_2$ fluorescence quantum dots for VB9 detection, achieving a LOD of 52 nM and a linear range of 0.03–33 μM. However, these methods have drawbacks. HPLC requires complicated and time-consuming sample preparation [16]. Electrochemical techniques and fluorescence analysis may experience decreased sensitivity in complex samples or environments [17–19]. Therefore, there is an urgent need for a rapid, accurate, and non-destructive method for the trace analysis of VC and VB9.

Terahertz (THz) waves, frequency ranging from 0.1 to 10 THz, are located between the infrared and millimeter wave regions. THz waves possess properties that distinguish them from other electromagnetic regions. Firstly, THz waves are characterized by millielectron volt level photon energies, which are insufficient to cause photoionization or damage biomolecules. This feature enables non-destructive detection [20,21]. Secondly, THz waves are highly sensitive to low-frequency motions of biomolecules, such as crystal vibrations and weak interactions. This property allows for molecular fingerprinting, enabling the precise identification of biomolecules [22]. Thirdly, THz waves demonstrate exceptional penetrability through non-metallic and non-polar materials. It facilitates non-destructive and non-contact detection [23,24]. Due to these inherent attributes, THz spectroscopy is a promising technology in the biomedical field, including the detection of vitamins. For instance, the intermolecular hydrogen bonds of vitamin B3, vitamin B6, and vitamin H have been resolved [25]. In the realm of quantitative detection, the detection of commercial VC tablets at the milligram level has been achieved, but the sensitivity remains an issue [26].

To overcome this sensitivity issue, researchers have developed THz metasurface biosensors, which are based on artificial composite structures comprising arrays [27]. Under the excitation of the incident THz waves, the resonator unit will generate various resonances, such as inductor-capacitor (LC) resonance [28], plasmon resonance [29,30], electromagnetic induced transparency (EIT) [31,32], absorption induced transparency [33], Fano resonance [34,35], etc. By altering the artificial unit structures, we can flexibly control the resonance peak and generate a strong local-field enhancement near the resonance frequency, which can improve the interaction between analytes and incident THz waves [36,37]. Thus, an increase in detection sensitivity can be achieved by measuring the frequency shift of the resonance peak caused by the change in the refractive index of the analyte [38,39]. A variety of THz metasurface biosensors have been developed for the detection of various analytes, such as viruses [40], proteins [41], and cells [42], offering the benefits of low sample consumption, high detection sensitivity, and simple sample pretreatment. Recent advancements have also shown promising applications in the detection of trace vitamins. The detection of vitamin B2 (VB2) and vitamin B6 (VB6) has been achieved; the LOD of

VB2 is 7.54 mg/mL and the detection range of VB6 is 0.015–0.125 mg/μL [43,44]. But the detection of VC and VB9 has not been reported.

This study aims to provide a novel detection method of VC and VB9 through the combination of THz spectroscopy with metasurface technology. We initially determined the characteristic absorption peaks and molecular vibration modes of VC and VB9 within the 0.5–4.0 THz range through terahertz time-domain spectroscopy (THz-TDS) measurements and quantum chemical calculations. A THz metasurface biosensor was then designed. Its resonance peak located at the common THz peak of both vitamins, enhancing the THz waves–vitamin molecules interaction. With this THz metasurface biosensor, we finally analyzed the peak shifts in response to varying concentrations of VC and VB9. This research offers a rapid, sensitive, and non-destructive method for vitamin detection. These findings are anticipated to advance efficient and convenient tools for food safety and clinical diagnostics.

## 2. Materials and Methods

### *2.1. Materials*

VC (CAS Number: 50-81-7, purity: Analytically Pure) and VB9 (CAS Number: 59-30-3, purity: ≥98%) were purchased from the Shanghai Aladdin Biochemical Technology Co. Ltd. (Shanghai, China). Copolymers of cycloolefin (COC) powder, with an average particle size below 60 μm, were purchased from the Shanghai Institute of Nuclear Research (Shanghai, China). These materials were used as received, without undergoing any additional purification. Purified water, with a resistivity of 18.4 MΩ·cm, was produced using a water purification system (PURELAB CLASSIC, ELGA, High Wycombe, UK).

### *2.2. Sample Preparation*

For qualitative detection, VC pellets (VC: 1 mg or 10 mg, COC: 60 mg) and VB9 pellets (VB9: 1 mg or 10 mg, COC: 60 mg) were prepared. The COC powder, known for its low absorption of THz waves, was used as a diluent. The detailed preparation process is as follows: 1 mg of VC powder was homogeneously mixed with 60 mg of COC powder. The mixture was then grinded and compressed under a pressure of 3 tons for 3 min to form a 1 mg VC pellet. A similar protocol was employed for the preparation of 10 mg VC pellet, 1 mg VB9 pellet and 10 mg VB9 pellet. Meanwhile, 60 mg of COC was compressed into a pellet for use as a reference sample. The preparation process was carefully controlled to keep material wastage below 1%. The resulting pellets had an average diameter of 13 mm and a thickness ranging from 500 to 580 μm.

For quantitative detection, a VC solution was prepared by dissolving 5 mg of VC powder in 5 mL of purified water, followed by thoroughly stirring. Aliquots were then diluted to obtain concentrations of 100, 200, 400, 600, 800, and 1000 ng/μL. Similar procedures were used to prepare VB9 solutions at equivalent concentrations. For THz spectroscopy analysis, 5 μL of each solution was dripped onto the center of the metasurface using an electronic pipette controller and an operator was ensured to follow a standardized protocol to ensure consistent results. The samples were then air-dried to form a uniformly thin film for further THz measurement, which takes about ten minutes for the samples to dry. After testing, the metasurface can be reused after rinsing the surface with purified water and wiping it clean.

### *2.3. THz Spectroscopy Measurement*

The THz experiments were conducted using a THz spectrometer (TAS7400, Advantest Ltd., Tokyo, Japan). The experimental setup is shown in Figure 1a and the operational principle is shown in Figure 1b. TAS7400 has an internal frequency reference of 50 MHz, which is the operation reference of the sampling timing circuit. Then, it employs two dual ultrashort pulse lasers for the generation and detection of THz waves. The output wavelength of the laser is 1550 nm, the output power is greater than 20 mW, and the pulse width is less than 50 fs. One laser sends pulses to the THz Emitter to trigger THz wave. The THz wave

passes through the examined sample, undergoing ratio measurement to extract the intrinsic information of the sample. Then, it is detected using a sampling wave emitted by another laser. The final step captures the sample's THz spectrum using free-space electro-optic sampling, followed by Analog to Digital (A/D) and Fast Fourier Transform (FFT).

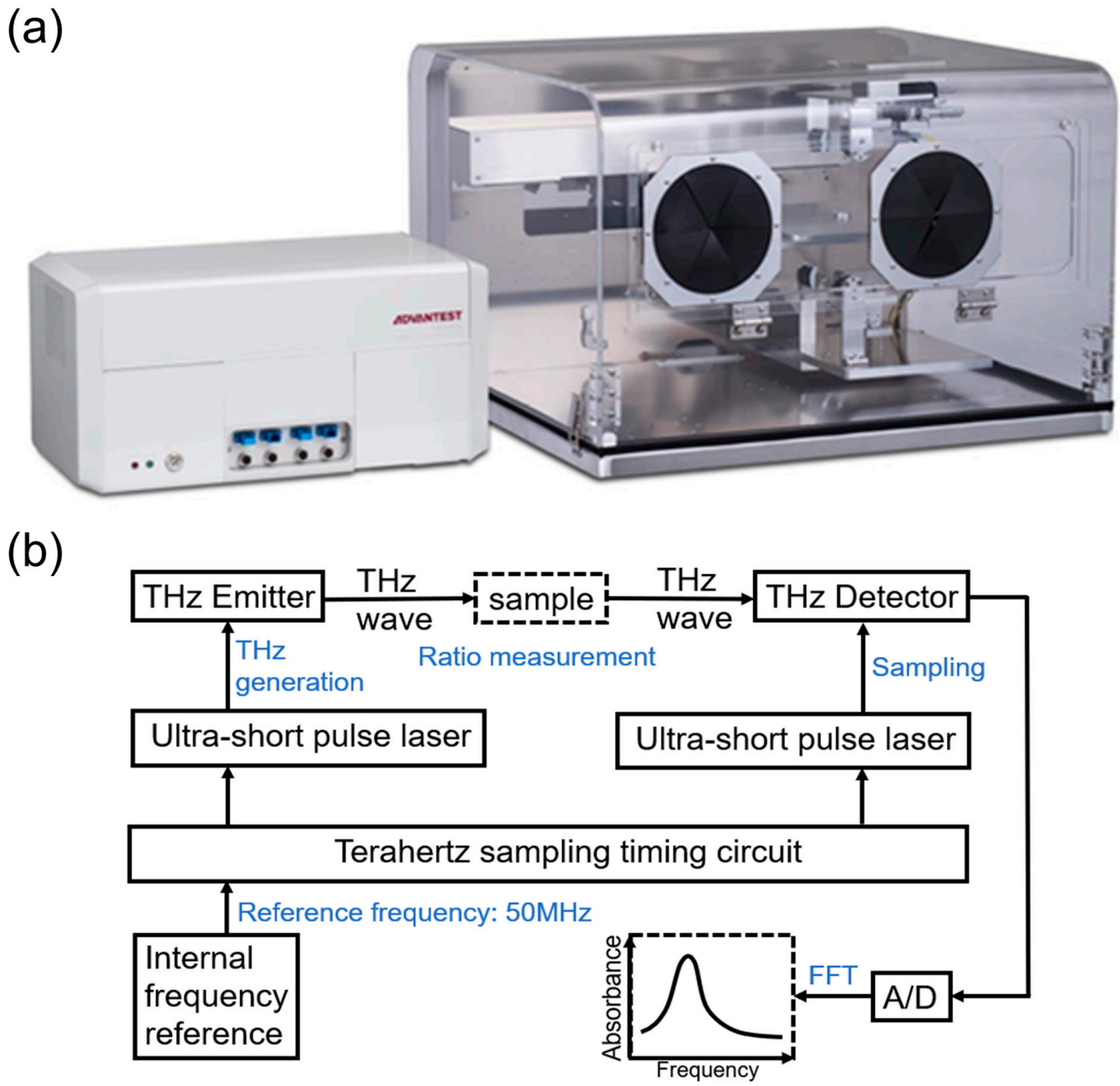


**Figure 1.** (**a**) Experimental setup and (**b**) its operational principle of the THz spectrometer.

This system had a dynamic range of 60 dB, a spot diameter of 5 mm, and an effective spectral range from 0.5 to 4.0 THz. Each THz spectrum was the result of 1024 cumulative acquisitions, providing a resolution of 1.9 GHz. To ensure reliability, each sample was measured in 4 repetitions to determine the error bars. The relative humidity of the sample chamber was kept below 3% by purging dry air to minimize the influence of water vapor. All experiments were conducted at 22 °C.

### *2.4. Theoretical Calculation*

The THz wave is highly sensitive to low-frequency molecular motions such as backbone vibrations and weak interactions. Therefore, it can reveal the unique molecular structure. To understand the characteristic absorption properties of VC and VB9 within the 0.5–4.0 THz range, quantum chemical calculations were conducted in this study. Density functional theory (DFT), a reliable quantum computational method, was employed. The DFT is particularly effective in predicting the vibrational frequencies of small- to medium-sized molecules [45].

The initial structural models for VC and VB9 were obtained from the PubChem database, with PubChem CID 54670067 for VC and 135398658 for VB9, respectively. These models were subsequently optimized, and their theoretical spectra and vibrational modes were calculated using Gaussian 09W software [46]. The vibration modes refer to the motion state of atoms or groups vibrating in a molecule. The theoretical vibrational modes of both VC and VB9 in the 0.5–4 THz range were analyzed using the DFT/B3LYP/6-31g(d) computational method. All vibrational frequencies were broadened with a full width at a half maximum (FWHM) of 4 $cm^{-1}$ to obtain their theoretical spectra.

## 3. Results and Discussion

### *3.1. Theoretical and Experimental Spectral Comparison of VC and VB9*

Figure 2a,c show the molecular structures of VC and VB9, respectively. Their vibrational modes and THz spectra in the 0.5–4.0 THz range were obtained using quantum chemical calculations, as shown in Figure 2b,d. The theoretical THz spectrum of VC exhibits four absorption peaks at 1.18, 1.78, 2.64, and 3.43 THz (Figure 2b), while the spectrum of VB9 displays six absorption peaks at 0.66, 1.09, 1.32, 1.72, 2.71, and 3.52 THz (Figure 2d).

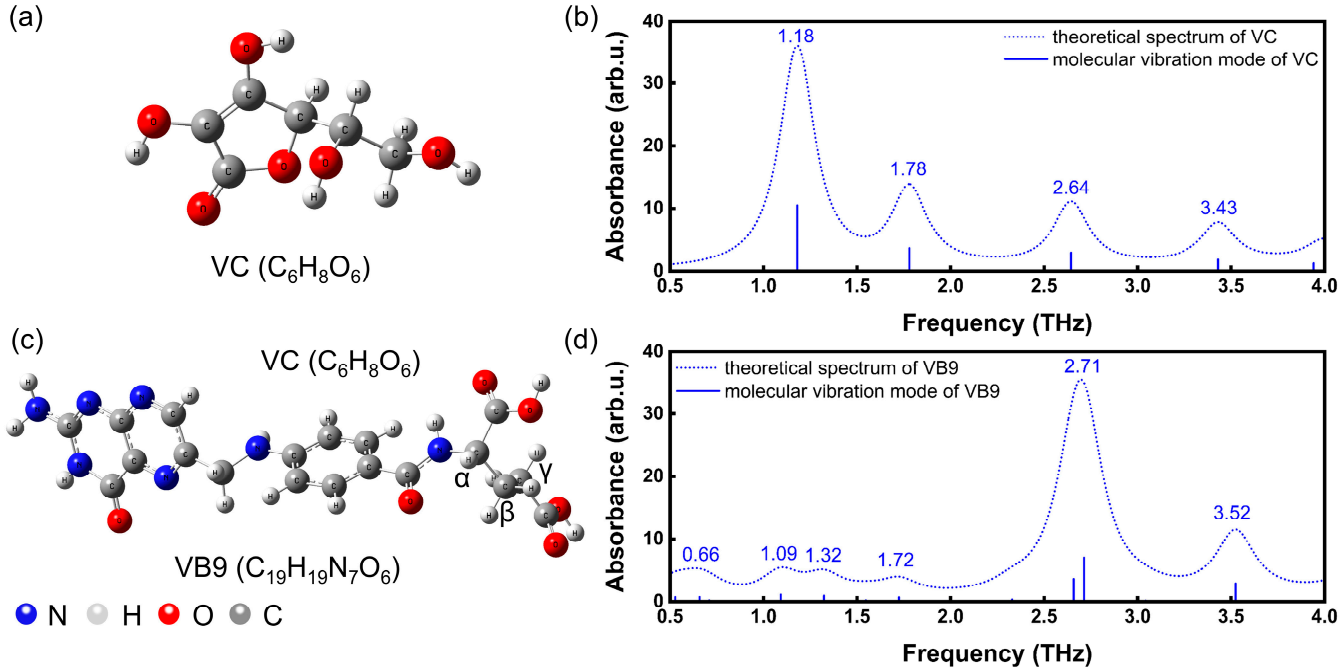


**Figure 2.** (**a**) Molecular structure and (**b**) theoretical THz spectra of VC; (**c**) molecular structure and (**d**) theoretical THz spectra of VB9.

Conventional THz spectroscopy typically involves analyzing samples in pellet form. We used a THz-TDS system to detect the spectra of both VC and VB9 pellets in the 0.5–4.0 THz range. The corresponding experimental spectra are shown in Figure 3a,b. For the 10 mg VC pellet, six absorption peaks are observed, including strong peaks at 1.75, 2.02, 2.29, and 3.53 THz, along with a weaker peak at 2.64 THz and a shoulder peak at 1.37 THz. The experimental peaks at 1.75, 2.64, and 3.53 THz correspond to the theoretical

peaks at 1.78, 2.64, and 3.43 THz, respectively, with an error not exceeding 0.10 THz. For the 10 mg VB9 pellet, four weak absorption peaks are observed at 1.54, 1.78, 2.79, and 3.52 THz. The experimental peaks at 1.78, 2.79, and 3.52 THz correspond to the theoretical peaks at 1.72, 2.71, and 3.52 THz, respectively, with an error not exceeding 0.08 THz.

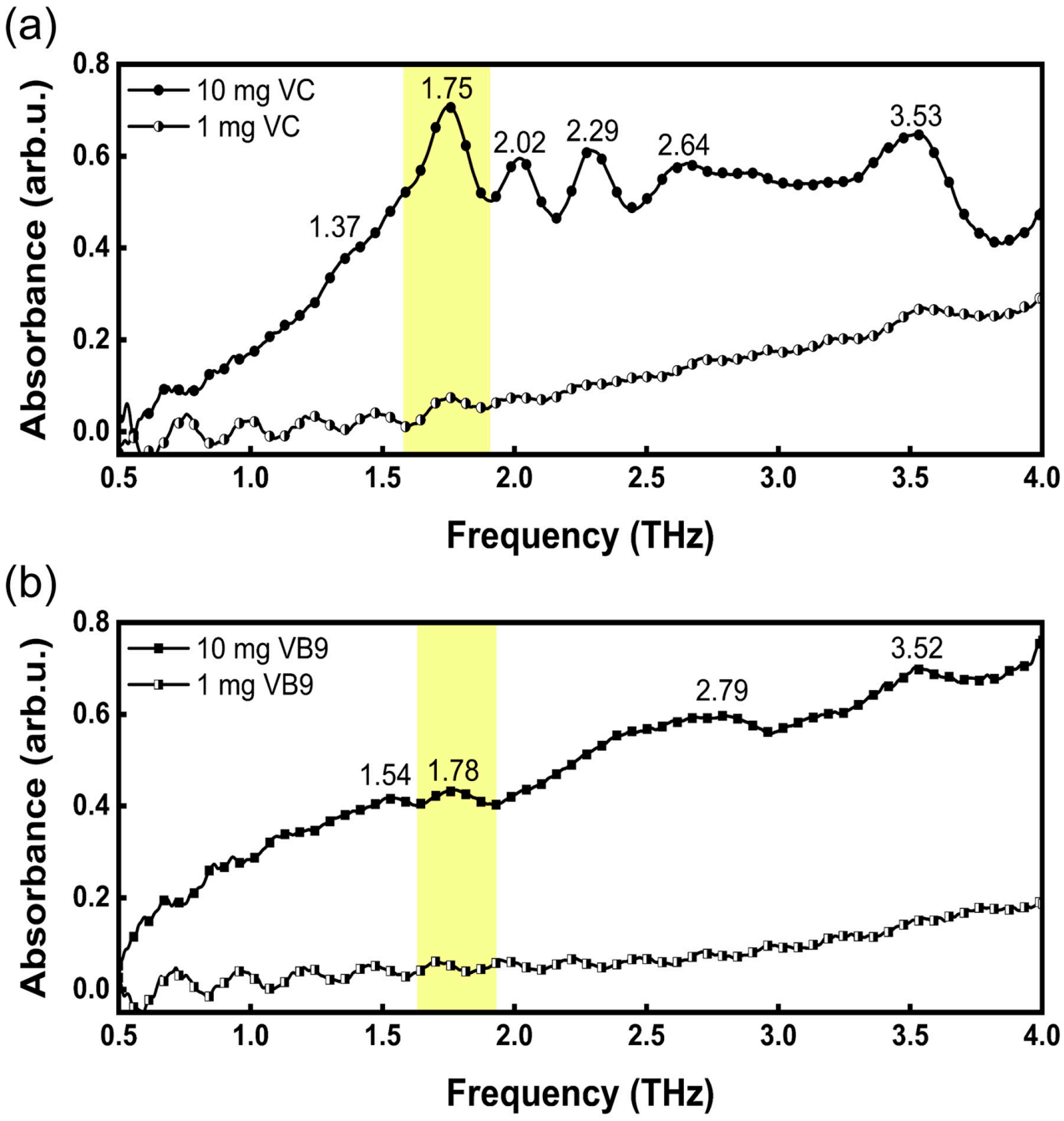


**Figure 3.** THz absorption spectrum of (**a**) VC and (**b**) VB9.

### *3.2. Vibrational Mode Assignment of VC and VB9*

The theoretical and experimental spectra exhibit excellent agreement within the 0.5–4.0 THz range. This allows us to identify the characteristic peaks for both VC and VB9. For VC, the experimental peaks at 1.75, 2.64, and 3.53 THz correspond to the theoretical peaks at 1.78, 2.64, and 3.43 THz, respectively. These peaks mainly arise from the twisting vibration of the hydroxymethyl group, but the vibration direction varies for each peak. For VB9, the experimental peak at 1.78 THz corresponds to the theoretical peak at

1.72 THz, mainly originating from the wagging vibration of the benzene ring and carboxyl group on the α-carbon. The experimental peak at 2.79 THz corresponds to the theoretical peak at 2.71 THz, mainly originating from the out-of-plane bending vibration of the pteridine ring and the in-plane bending vibration of the benzene ring. The experimental peak at 3.52 THz corresponds to the theoretical peak at 3.52 THz, mainly originating from the wagging vibration of the two methylene groups. Table 1 shows the statistics the vibrational modes of the different peaks of VC and VB9.

**Table 1.** The vibrational modes of the different peaks of VC and VB9.

| Vitamin | Theoretical Peak (THz) | Experimental Peak (THz) | Vibrational Mode * |
|---|---|---|---|
| VC | 1.75 | 1.78 | tw(−$CH_2OH$) |
| | 2.64 | 2.64 | tw(−$CH_2OH$) |
| | 3.53 | 3.43 | tw(−$CH_2OH$) |
| VB9 | 1.78 | 1.72 | w(-Ph-) + w(−COOH on α-carbon) |
| | 2.79 | 2.71 | op(-pteridine ring) + ip (-Ph-) |
| | 3.52 | 3.52 | w(β-$CH_2$-) + w(γ-$CH_2$-) |

* w, wagging; tw, twisting; op, out-of-plane bending; ip, in-plane bending; Ph, benzene ring; P, pteridine ring.

Parts of the experimental peaks lack corresponding theoretical peaks, for instance, the experimental peaks of VC at 2.02 and 2.29 THz. This phenomenon may be attributed to the differences in conditions between theoretical calculation and experimental measurement. Theoretical calculation is performed on isolated molecules at 0 K, while experimental measurements are conducted on polymolecule systems at room temperature, thus affecting the accuracy of low-frequency molecular mode analysis in the THz region [45].

However, when the vitamin content was reduced to 1 mg, the THz absorption peaks for both VC and VB9 became very weak, as illustrated in Figure 3a,b. The weak peaks are difficult to recognize efficiently, significantly limiting the detection sensitivity. To address this issue, we combined THz spectroscopy with a metasurface biosensor to detect trace amounts of VC and VB9. The experimental peaks at 1.75 THz for VC and 1.78 THz for VB9 (highlighted by the yellow bands in Figure 3) can serve as the resonance enhancement band in guiding the metasurface design.

### *3.3. Design and Fabrication of THz Metasurface Biosensor*

The metasurface consists of two ring chain resonators, each with different gap widths. The unit structure and its periodic arrangement of the metasurface are shown in Figure 4a,b, respectively. The resonators are made of gold (thickness: 200 nm) and placed on a quartz substrate (thickness, h: 500.00 μm). The geometric parameters of the resonators are as follows: $p_x$ = 37.00 μm, $p_y$ = 74.00 μm, w = 5.00 μm, $d_1$ = 20.00 μm, $d_2$ = 7.00 μm, $g_1$ = 2.00 μm, and $g_2$ = 4.00 μm. The theoretical simulation of the unit structure was performed using COMSOL Multiphysics 6.1 software. The electric field distribution at 1.74 THz is shown in Figure 4c. The electric field is mainly concentrated in the relatively narrow metal ring gap. The theoretical spectrum is shown in Figure 4d. The theoretical resonance peak is located at 1.74 THz, at around the common absorption peaks of VC and VB9 (1.75 THz and 1.78 THz). The FWHM of the resonance peak is 0.013 THz. The Q-factor is calculated to be 133.8. In Table 2, we compare the Q-factors of the THz metal-based metasurfaces found in recent years. These metasurfaces have different resonance types. Table 2 shows that our designed metasurface possesses a relatively high Q-factor. The relatively high Q-factor indicates that there is great energy density within the metasurface, making it more sensitive to electromagnetic field changes. This resonance can enhance interaction between vitamin molecules and THz waves specifically at this frequency, thereby enhancing detection sensitivity for VC and VB9.

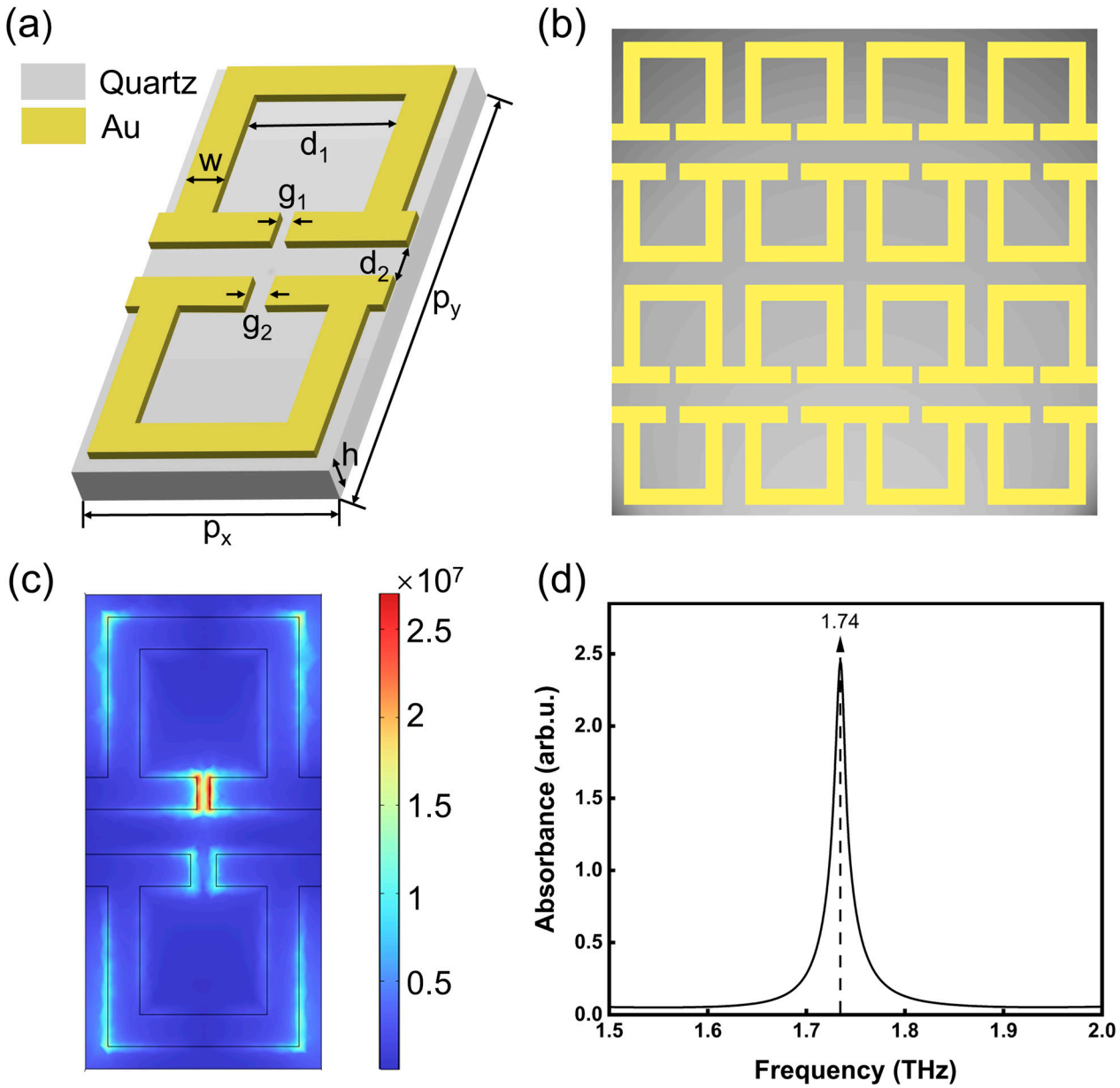


**Figure 4.** (**a**) Schematic of the unit structure; (**b**) periodic structure of the metasurface biosensor; (**c**) electric field distribution diagram; and (**d**) theoretical spectrum of the metasurface biosensor simulated using COMSOL Multiphysics 6.1 software.

The metasurface was fabricated using lithography techniques, with quartz substrate, gold resonators, and a chromium layer. Figure 5a shows the optical images of the metasurface biosensor and its actual geometric parameters. Figure 5b presents its measured THz spectrum. It displays a resonance peak at 1.77 THz with a FWHM of 0.169 THz, resulting in an actual Q-factor of 10.5. The measured resonance peak closely matches the theoretical peak (1.74 THz), with a slight deviation due to machining limitations resulting in a difference between the actual and the theoretical parameters (less than 0.22 μm). Moreover, the theoretical simulation considered gold as a perfect electrical conductor, which differs from the actual properties of gold. Despite these differences, the measured resonance peak at 1.77 THz corresponded well with the characteristic peaks of VC at 1.75 THz and VB9 at 1.78 THz. This indicates effective enhancement effects between the sample and THz waves.

**Table 2.** Comparison of Q-factor of THz metasurface in recent years.

| Year | Resonator Material | Resonance Type | Resonance Peak (THz) | Q-Factor | Reference |
|---|---|---|---|---|---|
| 2021 | Al | LC resonance | 0.84 | 10.6 | [47] |
| 2021 | Au | EIT resonance | 0.94 | 24.6 | [48] |
| | | | 1.56 | 100.7 | |
| 2022 | Au | Toroidal resonance | 2.39 | 15.2 | [49] |
| 2022 | Al | Fano resonance | 0.94 | 64 | [50] |
| 2023 | Au | Plasmon resonance | 1.97 | 19.1 | [51] |
| | | | 3.37 | 156.0 | |
| 2023 | Cu | Magnetic dipole resonance | 0.47 | 55.3 | [52] |
| 2024 | Au | Plasmon resonance | 1.74 | 133.8 | This work |

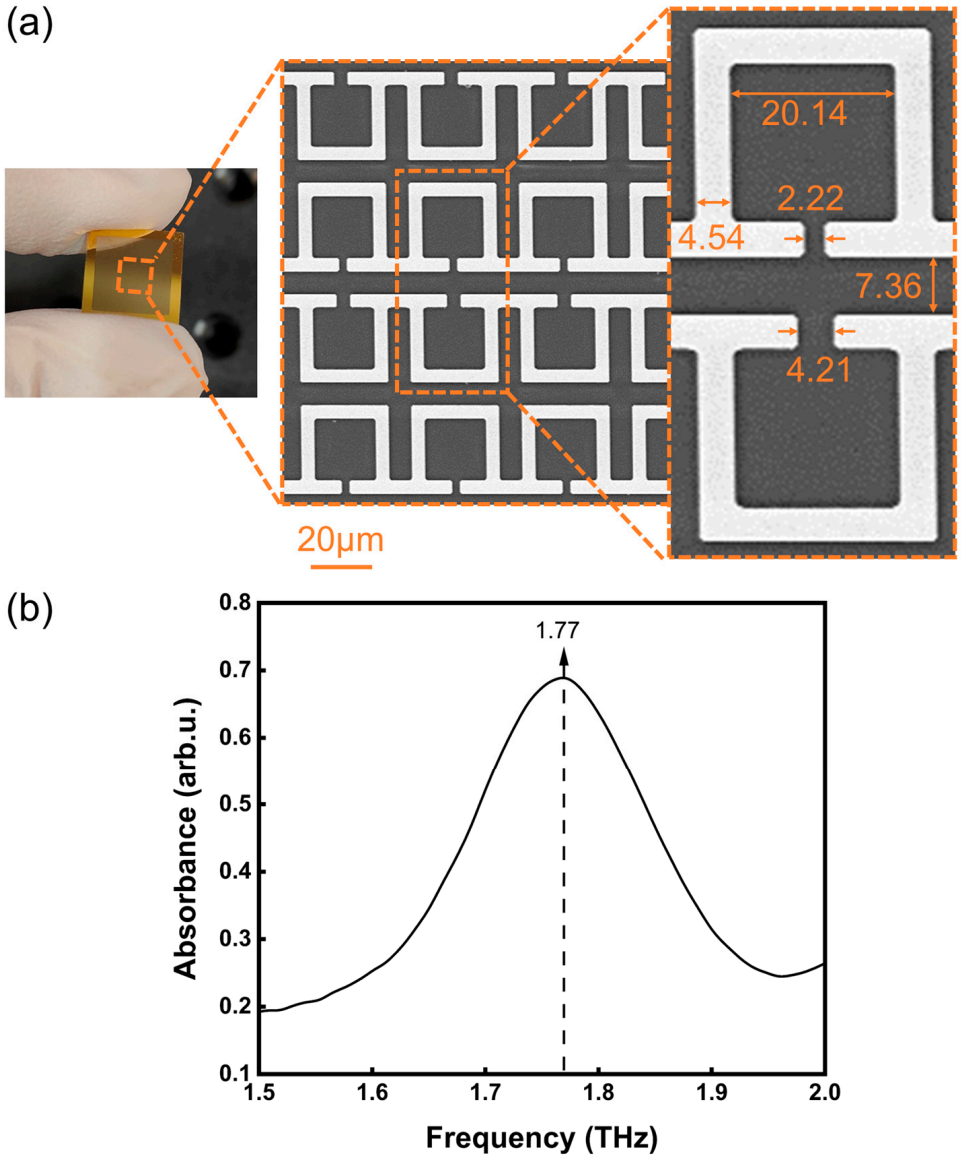


**Figure 5.** (**a**) Optical micrograph and actual geometric parameters of the fabricated metasurface biosensor, and (**b**) measured spectrum of the metasurface biosensor in the 1.5–2.0 THz range.

### *3.4. Detection of VC and VB9 Based on THz Metasurface Biosensor*

When a metasurface is coated with a sample, the dielectric constant of the metasurface changes, causing a shift in its resonance frequency. Variations in sample concentration result in different frequency shifts, enabling quantitative analysis [53]. We prepare VC and VB9 samples at concentrations ranging from 0 to 1000 ng/μL, respectively. Subsequently, we pipette 5 μL of each sample onto the metasurface. After thorough drying, the samples form a uniform thin layer on the metasurface. We then analyze their absorbance spectra within the 0.5–4.0 THz range, focusing on the resonance peaks centered at approximately 1.75 THz.

Figure 6a shows the resonance peak of the VC samples of varying concentrations. The average resonance peaks are at 1.7662 THz (0 ng/μL), 1.7636 THz (100 ng/μL), 1.7552 THz (200 ng/μL), 1.7546 THz (400 ng/μL), 1.7476 THz (600 ng/μL), 1.7464 THz (800 ng/μL), and 1.7431 THz (1000 ng/μL). It is evident that the resonance peak gradually shifts to lower frequencies as the concentration of VC increases. To further quantify the relationship between VC concentration and frequency shift, we plot the frequency shifts, depicted by the hollow circles in Figure 6b. The data suggest a nonlinear correlation, which is modeled using a nonlinear fit, as shown in Figure 6b. The fitted equation is as follows:

$$y = -(0.031 \pm 0.0079) \times \exp[(-0.0014 \pm 0.0027)x] + (0.031 \pm 0.0087), R^2 = 0.96 \quad (1)$$

where x represents the VC concentration, y represents the frequency shift caused by the VC on the metasurface, and $R^2$ is the determination coefficient of the fitted curve. $R^2$ is 0.96, indicating a good fit of the data to the nonlinear model. Based on this model, we can achieve the quantitative detection of VC by monitoring the frequency shift of the metasurface. It can be observed that the frequency shift intensifies with concentration, but the rate of increase attenuates. This attenuation is attributed to the increased thickness of the dried sample film at higher concentrations, which diminishes the impact of the sample on the overall equivalent capacitance of the metasurface and consequently decreases the frequency shift. The limit of detection (LOD) for VC is calculated using the following formula:

$$\mathrm{LOD} = \frac{3.3\,\delta}{S} \quad (2)$$

where δ represents the standard deviation of the data obtained without sample, specifically indicating the variability in resonance frequency when the sample concentration is 0 ng/μL. S represents the maximum slope observed in the fitted curve. For VC detection, LOD is determined to be 158.82 ng/μL.

Figure 6c shows the resonance peak of VB9 samples of varying concentrations. The average resonance peaks are at 1.7684 (0 ng/μL), 1.7651 (100 ng/μL), 1.7633 (200 ng/μL), 1.7625 (400 ng/μL), 1.7577 (600 ng/μL), 1.7535 (800 ng/μL), and 1.7489 (1000 ng/μL) THz. There is a clear tendency for the frequency of the resonance peak to decrease as the concentration of VB9 increases. The frequency shifts for VB9 samples, represented by hollow squares in Figure 6d, exhibit a linear relationship with concentration. A linear regression analysis is conducted to derive the fitting curve shown in Figure 6d, with the fitting equation given by the following:

$$y = (1.82 \times 10^{-5} \pm 1.28 \times 10^{-6})\,x + (4.21 \times 10^{-4} \pm 4.21 \times 10^{-4}), R^2 = 0.98 \quad (3)$$

where x is the concentration of the VB9, y is the frequency shift induced by the VB9, and $R^2$ is the determination coefficient of the fitted curve. $R^2$ is 0.98, indicating a strong linear relationship. As the concentration of VB9 increases, so does the frequency shift of the metasurface. Notably, this increase does not diminish over the concentration range studied. This behavior is different than that observed for VC, possibly due to the lower sample concentrations of VB9 that have not yet reached saturation. For VB9 detection, LOD is determined to be 353.57 ng/μL.

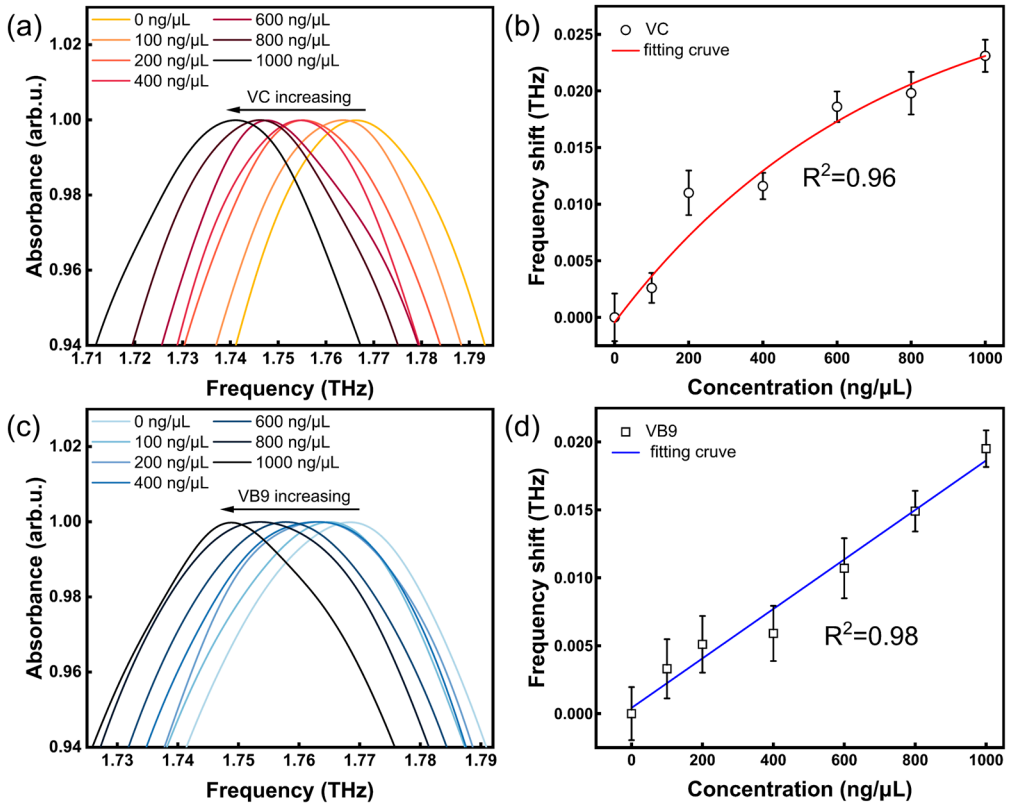


**Figure 6.** (**a**) THz absorption spectra for varying VC concentrations, and (**b**) the relationship between the frequency shift of the metasurface and VC concentrations; (**c**) THz absorption spectra for varying VB9 concentrations, and (**d**) the relationship between the frequency shift of the metasurface and VB9 concentrations.

These findings illustrate that integrating THz spectroscopy with a metasurface allows for the detection of trace VC and VB9. This method facilitates rapid and non-destructive detection.

## 4. Conclusions

This study proposes a fast, sensitive, and non-destructive detection method for the trace analysis of vitamins by combining THz spectroscopy with metasurface technology. Firstly, we identified the THz characteristic peaks of VC and VB9 through DFT calculations and THz spectroscopy. Then, we designed and fabricated a metasurface biosensor with a resonance peak at 1.77 THz, which well-matched with the characteristic peaks of VC at 1.75 THz and VB9 at 1.78 THz. This metasurface biosensor significantly enhances the interaction between the samples and the THz wave, thereby improving detection sensitivity. With this metasurface biosensor, we successfully detect VC and VB9 solutions at different concentrations. By analyzing the frequency shifts in relation to concentration changes, we were able to rapidly identify VC and VB9 in 0–800 ng/μL range. The LODs were determined to be 158.82 ng/μL for VC and 353.57 ng/μL for VB9. This study demonstrates the potential of combining a metasurface with THz spectroscopy for trace analysis, providing a viable approach for the simple, rapid, and non-destructive detection of vitamins.

**Author Contributions:** Conceptualization, X.W. and Y.P.; methodology, X.W.; software, N.W. and B.L.; formal analysis, N.W.; investigation, N.W. and B.L.; writing—original draft preparation, N.W.; writing—review and editing, X.W.; visualization, N.W.; supervision, X.W.; funding acquisition, Y.P. and X.W. All authors have read and agreed to the published version of the manuscript.

**Funding:** This research was funded by National Natural Science Foundation of China (NSFC) [grant number 61988102, 61805140, 62335012] and National Key Research and Development Program of China [grant number 2022YFA1404004, 2023YFF0719200]. The high-performance computing

resources and services used in this work were supported by the High-Performance Computing Center, University of Shanghai for Science and Technology.

**Institutional Review Board Statement:** Not applicable.

**Informed Consent Statement:** Not applicable.

**Data Availability Statement:** Data underlying the results presented in this paper are not publicly available at this time but may be obtained from the authors upon reasonable request.

**Conflicts of Interest:** There are no conflicts of interest to declare.

## References

1. Calder, P.C.; Carr, A.C.; Gombart, A.F.; Eggersdorfer, M. Optimal Nutritional Status for a Well-Functioning Immune System Is an Important Factor to Protect against Viral Infections. *Nutrients* **2020**, *12*, 1181. [CrossRef]
2. Tardy, A.L.; Pouteau, E.; Marquez, D.; Yilmaz, C.; Scholey, A. Vitamins and Minerals for Energy, Fatigue and Cognition: A Narrative Review of the Biochemical and Clinical Evidence. *Nutrients* **2020**, *12*, 228. [CrossRef]
3. Fowler, A.A. Vitamin C: Rationale for Its Use in Sepsis-Induced Acute Respiratory Distress Syndrome (ARDS). *Antioxidants* **2024**, *13*, 95. [CrossRef]
4. Isola, S.; Gammeri, L.; Furci, F.; Gangemi, S.; Pioggia, G.; Allegra, A. Vitamin C Supplementation in the Treatment of Autoimmune and Onco-Hematological Diseases: From Prophylaxis to Adjuvant Therapy. *Int. J. Mol. Sci.* **2024**, *25*, 7284. [CrossRef] [PubMed]
5. Doseděl, M.; Jirkovský, E.; Macáková, K.; Krčmová, L.K.; Javorská, L.; Pourová, J.; Mercolini, L.; Remião, F.; Nováková, L.; Mladěnka, P.; et al. Vitamin C—Sources, Physiological Role, Kinetics, Deficiency, Use, Toxicity, and Determination. *Nutrients* **2021**, *13*, 615. [CrossRef] [PubMed]
6. Kancherla, V.; Botto, L.D.; Rowe, L.A.; Shlobin, N.A.; Caceres, A.; Smith, A.A.; Zimmerman, K.; Blount, J.; Kibruyisfaw, Z.; Ghotme, K.A.; et al. Preventing birth defects, saving lives, and promoting health equity: An urgent call to action for universal mandatory food fortification with folic acid. *Lancet Glob. Health* **2022**, *10*, 1053–1057. [CrossRef]
7. Nawaz, F.Z.; Kipreos, E.T. Emerging roles for folate receptor FOLR1 in signaling and cancer. *Trends Endocrinol. Metab.* **2022**, *33*, 159–174. [CrossRef] [PubMed]
8. Zwart, N.R.K.; Franken, M.D.; Tissing, W.J.E.; Lubberman, F.J.E.; McKay, J.A.; Kampman, E.; Kok, D.E. Folate, folic acid, and chemotherapy-induced toxicities: A systematic literature review. *Crit. Rev. Oncol./Hematol.* **2023**, *188*, 104061. [CrossRef] [PubMed]
9. Shulpekova, Y.; Nechaev, V.; Kardasheva, S.; Sedova, A.; Kurbatova, A.; Bueverova, E.; Kopylov, A.; Malsagova, K.; Dlamini, J.C.; Ivashkin, V. The Concept of Folic Acid in Health and Disease. *Molecules* **2021**, *26*, 3731. [CrossRef]
10. Li, H.; Li, L.; Qian, X.; Zhang, J.; Zheng, Z.; Chen, Y. Simultaneous determination of organic acids and VC content in fruits and vegetables using high performance liquid chromatography. *Hubei Agric. Sci.* **2024**, *63*, 171–175+184. [CrossRef]
11. Yang, Y.; Shi, K.; Liu, Z.; Xu, Z. The determination of folie acid in drug and food by high performanceliquid chromatography. *Chem. Res. Appl.* **2024**, *36*, 910–915.
12. Brainina, K.Z.; Bukharinova, M.A.; Stozhko, N.Y.; Sokolkov, S.V.; Tarasov, A.V.; Vidrevich, M.B. Electrochemical Sensor Based on a Carbon Veil Modified by Phytosynthesized Gold Nanoparticles for Determination of Ascorbic Acid. *Sensors* **2020**, *20*, 1800. [CrossRef] [PubMed]
13. Kuceki, M.; de Oliveira, F.M.; Segatelli, M.G.; Coelho, M.K.L.; Pereira, A.C.; da Rocha, L.R.; Mendonça, J.C.; Tarley, C.R.T. Selective and sensitive voltammetric determination of folic acid using graphite/restricted access molecularly imprinted poly(methacrylic acid)/$SiO_2$ composite. *J. Electroanal. Chem.* **2018**, *818*, 223–230. [CrossRef]
14. Wang, Y.; Yang, Y.; Liu, W.; Ding, F.; Zou, P.; Wang, X.; Zhao, Q.; Rao, H. A carbon dot-based ratiometric fluorometric and colorimetric method for determination of ascorbic acid and of the activity of ascorbic acid oxidase. *Microchim. Acta* **2019**, *186*, 246. [CrossRef]
15. May, B.M.M.; Parani, S.; Rajendran, J.V.; Oluwafemi, O.S. Selective detection of folic acid in the midst of other biomolecules using water-soluble $AgInS_2$ quantum dots. *MRS Commun.* **2019**, *9*, 1306–1310. [CrossRef]
16. Isane, S.P.; Waghmare, S.A.; Kamble, H.V. A Review on Method Development, Validation, Optimization and Applications of HPLC. *Int. J. Res. Appl. Sci. Eng. Technol.* **2022**, *10*, 1860–1867. [CrossRef]
17. Lakard, S.; Pavel, I.A.; Lakard, B. Electrochemical Biosensing of Dopamine Neurotransmitter: A Review. *Biosensors* **2021**, *11*, 179. [CrossRef] [PubMed]
18. Ferreira, M.d.P.; Yamada-Ogatta, S.F.; Teixeira Tarley, C.R. Electrochemical and Bioelectrochemical Sensing Platforms for Diagnostics of COVID-19. *Biosensors* **2023**, *13*, 336. [CrossRef]
19. Jing, Z.; Wang, W.; Nong, Y.; Zhu, P.; Lu, Y.; Wu, Q. Fluorescence analysis for water characterization: Measurement processes, influencing factors, and data analysis. *Water Reuse* **2022**, *13*, 33–50. [CrossRef]
20. Chen, H.; Han, J.; Liu, J.; Gao, L.; Ma, S. Identification of chiral lansoprazole drugs using THz fingerprint spectroscopy. *Chem. Pap.* **2022**, *77*, 887–893. [CrossRef]
21. Zhang, S.; Chen, X.; Liu, K.; Li, H.; Xu, Y.; Jiang, X.; Xu, Y.; Wang, Q.; Cao, T.; Tian, Z. Nonvolatile reconfigurable terahertz wave modulator. *PhotoniX* **2022**, *3*, 7. [CrossRef]

22. Smolyanskaya, O.A.; Chernomyrdin, N.V.; Konovko, A.A.; Zaytsev, K.I.; Ozheredov, I.A.; Cherkasova, O.P.; Nazarov, M.M.; Guillet, J.-P.; Kozlov, S.A.; Kistenev, Y.V.; et al. Terahertz biophotonics as a tool for studies of dielectric and spectral properties of biological tissues and liquids. *Prog. Quantum Electron.* **2018**, *62*, 1–77. [CrossRef]
23. Hu, X.; Zhou, L.; Wu, X.; Peng, Y. Review on near-field detection technology in the biomedical field. *Adv. Photonics Nexus* **2023**, *2*, 044002. [CrossRef]
24. Shi, C.; Xu, W.; Peng, Y. Applications of terahertz imaging technology in tumor detection. *Opto-Electron. Eng.* **2020**, *47*, 190638. [CrossRef]
25. Takahashi, M.; Okamura, N.; Ding, X.; Shirakawaa, H.; Minamide, H. Intermolecular hydrogen bond stretching vibrations observed in terahertz spectra of crystalline vitamins. *CrystEngComm* **2018**, *20*, 1960–1969. [CrossRef]
26. Kang, J.; Song, J.; Jung, T.S.; Kwak, K.; Chun, H.S. In-Situ Measurement of Vitamin C Content in Commercial Tablet Products by Terahertz Time-Domain. *J. Infrared Millim. Terahertz Waves* **2018**, *39*, 367–377. [CrossRef]
27. Trainiti, G.; Xia, Y.W.; Marconi, J.; Cazzulani, G.; Erturk, A.; Ruzzene, M. Time-Periodic Stiffness Modulation in Elastic Metamaterials for Selective Wave Filtering: Theory and Experiment. *Phys. Rev. Lett.* **2019**, *122*, 124301. [CrossRef] [PubMed]
28. Ma, Y.; Xu, Y.; Sheng, H.; Chen, X.; Li, R.; Chen, Q.; Chou, X.; Chen, Q.; Vickers, A.; Akbar, J.; et al. THz-Metasurface Device with Multiple Resonance Modes. *Semicond. Optoelectron.* **2024**, *45*, 181. [CrossRef]
29. Singh, Y.; Mishra, A.C.; Yadav, S.; Jaiswal, L.; Lohia, P.; Dwivedi, D.K.; Yadav, R.K.; Eldesoky, G.E.; Hossain, M.K. High-Performance Plasmonic Biosensor for Blood Cancer Detection: Achieving Ultrahigh Figure-of-Merit. *Plasmonics* **2024**, 9. [CrossRef]
30. Nie, A.; He, X.; Cao, W. Carbon-based ultrabroadband tunable terahertz metasurface absorber. *Adv. Photonics Nexus* **2024**, *3*, 016007. [CrossRef]
31. Fu, W.; Sun, L.; Cao, H.; Chen, L.; Zhou, M.; Shen, S.; Zhu, Y.; Zhuang, S. Qualitative and Quantitative Recognition of Volatile Organic Compounds in Their Liquid Phase Based on Terahertz Microfluidic EIT Meta-Sensors. *IEEE Sens. J.* **2023**, *23*, 12775–12784. [CrossRef]
32. Men, K.; Lian, Z.; Tu, H.; Zhao, H.; Wei, Q.; Jin, Q.; Mao, C.; Wei, F. An All-Dielectric Metamaterial Terahertz Biosensor for Cytokine Detection. *Micromachines* **2024**, *15*, 53. [CrossRef] [PubMed]
33. Lyu, J.; Shen, S.; Chen, L.; Zhu, Y.; Zhuang, S. Frequency selective fingerprint sensor: The Terahertz unity platform for broadband chiral enantiomers multiplexed signals and narrowband molecular AIT enhancement. *PhotoniX* **2023**, *4*, 28. [CrossRef]
34. Yan, X.; Liang, L.; Yan, R.; Wu, G.; Yao, H.; Li, Z.; Wang, Z.; Hu, X.; Li, Y.; Zhang, Y. Fano resonance-integrated metal nanoparticles' enhanced sensing for pesticide detection. *Opt. Express* **2024**, *32*, 1295–1304. [CrossRef] [PubMed]
35. Wang, R.; Xu, L.; Wang, J.; Sun, L.; Jiao, Y.; Meng, Y.; Chen, S.; Chang, C.; Fan, C. Electric Fano resonance-based terahertz metasensors. *Nanoscale* **2021**, *13*, 18467–18472. [CrossRef]
36. Liu, B.; Peng, Y.; Hao, Y.; Zhu, Y.; Chang, S.; Zhuang, S. Ultra-wideband terahertz fingerprint enhancement sensing and inversion model supported by single-pixel reconfigurable graphene metasurface. *PhotoniX* **2024**, *5*, 10. [CrossRef]
37. Shih, K.L.; Pitchappa, P.; Jin, L.; Chen, C.; Singh, R.; Lee, C. Nanofluidic terahertz metasensor for sensing in aqueous environment. *Appl. Phys. Lett.* **2018**, *113*, 071105. [CrossRef]
38. Salehnezhad, Z.; Soroosh, M.; Mondal, H. A Highly Sensitive Plasmonic Graphene-Based Structure for Deoxyribonucleic Acid Detection. *Photonics* **2024**, *11*, 549. [CrossRef]
39. Gao, S.; Li, H.; Liu, L.; Tian, Y.; Wang, F.; Pan, X.; Wen, F.; Xiang, J.; Nie, A.; Zhai, K.; et al. Ultrasensitive CCL2 Detection in Urine for Diabetic Nephropathy Diagnosis Using a WS2-Based Plasmonic Biosensor. *Nano Lett.* **2024**, *24*, 5301–5307. [CrossRef]
40. Sengupta, R.; Khand, H.; Sarusi, G. Terahertz impedance spectroscopy of biological nanoparticles by a resonant metamaterial chip for breathalyzer-based COVID-19 prompt tests. *Nano Mater* **2022**, *5*, 5803–5812. [CrossRef]
41. Lee, S.; Lee, Y.; Lee, S.; Lee, S.; Kwak, J.; Song, H.S.; Seo, M. Detection and discrimination of SARS-CoV-2 spike protein-derived peptides using THz metamaterials. *Biosens. Bioelectron.* **2022**, *202*, 113981. [CrossRef] [PubMed]
42. Bai, Z.; Liu, Y.; Kong, R.; Nie, T.; Sun, Y.; Li, H.; Sun, T.; Pandey, C.; Wang, Y.; Zhang, H.; et al. Near-field terahertz sensing of hela cells and pseudomonas based on monolithic integrated metamaterials with a spintronic terahertz emitter. *Nano Mater.* **2020**, *12*, 35895–35902. [CrossRef]
43. Wang, Y.; Qin, B.; Li, Z.; Li, D.; Hu, F.; Zhang, H.; Yu, L. Analysis of reaction between vitamin B6 and bovine serum albumin based on a terahertz metamaterial sensor. *Appl. Opt.* **2022**, *61*, 7978–7984. [CrossRef] [PubMed]
44. Huang, L.; Cao, H.; Chen, L.; Ma, Y.; Yang, Y.; Liu, X.; Wang, W.; Zhu, Y.; Zhuang, S. Terahertz reconfigurable metasensor for specific recognition multiple and mixed chemical substances based on AIT fingerprint enhancement. *Talanta* **2024**, *269*, 125481. [CrossRef] [PubMed]
45. Wan, M.; Fang, J.; Xue, J.; Liu, J.; Qin, J.; Hong, Z.; Li, J.; Du, Y. Pharmaceutical Cocrystals of Ethenzamide: Molecular Structure Analysis Based on Vibrational Spectra and DFT Calculations. *Int. J. Mol. Sci.* **2022**, *23*, 8850. [CrossRef]
46. Frisch, M.J.; Trucks, G.W.; Schlegel, H.B.; Scuseria, G.E.; Robb, M.A.; Cheeseman, J.R.; Scalmani, G.; Barone, V.; Petersson, G.A.; Nakatsuji, H.; et al. *Gaussian 09, Revision D.01*; Gaussian, Inc.: Wallingford, CT, USA, 2016.
47. Hou, X.; Chen, X.; Li, T.; Li, Y.; Tian, Z.; Wang, M. Highly sensitive terahertz metamaterial biosensor for bovine serum albumin (BSA) detection. *Opt. Mater. Express* **2021**, *11*, 2268–2277. [CrossRef]
48. Zhu, L.; Li, H.; Dong, L.; Zhou, W.; Rong, M.; Zhang, X.; Guo, J. Dual-band electromagnetically induced transparency (EIT) terahertz metamaterial sensor. *Opt. Mater. Express* **2021**, *11*, 2109–2121. [CrossRef]

49. Zhang, C.; Xue, T.; Zhang, J.; Liu, L.; Xie, J.; Wang, G.; Yao, J.; Zhu, W.; Ye, X. Terahertz toroidal metasurface biosensor for sensitive distinction of lung cancer cells. *Nanophotonics* **2022**, *11*, 101–109. [CrossRef]
50. Cen, W.; Lang, T.; Hong, Z.; Liu, J.; Xiao, M.; Zhang, J.; Yu, Z. Ultrasensitive Flexible Terahertz Plasmonic Metasurface Sensor Based on Bound States in the Continuum. *IEEE Sens. J.* **2022**, *22*, 12838–12845. [CrossRef]
51. EL-Wasif, Z.; Ismail, T.; Hamdy, O. Design and optimization of highly sensitive multi-band terahertz metamaterial biosensor for coronaviruses detection. *Opt. Quantum Electron.* **2023**, *55*, 604. [CrossRef] [PubMed]
52. Qu, Z.; Kang, J.; Li, W.; Yao, B.; Deng, H.; Wei, Y.; Jing, H.; Li, X.; Duan, J.; Zhang, B. Microstructure-based high-quality factor terahertz metamaterial bio-detection sensor. *Adv. Compos. Hybrid Mater.* **2023**, *6*, 100. [CrossRef]
53. Zhang, W.; Lin, J.; Yuan, Z.; Lin, Y.; Shang, W.; Chin, L.K.; Zhang, M. Terahertz Metamaterials for Biosensing Applications: A Review. *Biosensors* **2024**, *14*, 3. [CrossRef] [PubMed]